Numerical Simulation of Autorotation

By

Naoki IZUTSU* and Yuko OSHIMA**

(January 25, 1984)

Summary: Autorotation of an elliptic cylinder around its spanwise axis fixed perpendicularly in a uniform flow was numerically simulated by using discrete vortex-blob method and compared with experimental results using wind tunnel and water channel. The flow fields around the cylinder driven externally with constant angular velocity were investigated, and the effects of the moment of inertia and of the thickness ratio of the cylinder on the starting condition of autorotation were analyzed, which clarified the mechanism of autorotation. That is, the driving force is due to shedding of the vortex clinging behind the retreating edge. The cylinders with sufficiently large moments of inertia rotate with constant angular velocity, whereas those with smaller one induce periodic variation of angular velocity. The cylinders with smaller moment of inertia than a critical value cannot sustain autorotation. It was also found that the autorotation frequency increases as the thickness ratio of the elliptic cylinder decreases, and eventually reaches the maximum values which is larger than the one of a flat plate.

1. INTRODUCTION

It is well known that a fallen rectangular card falls obliquely in air, having been rotating around one of its spanwise axes. This so-called autorotation phenomenon is defined as continuous rotation of a symmetrical body without mechanical force. Such a body has one or more stable neutral attitudes at which no torque at resting state acts, and also can autorotate around the fixed axis, if sufficiently strong initial drive to start is applied.

Autorotation phenomena have been extensively investigated by many authors [*1–4*]. Smith [*1*] studied experimentally over a wide range of Reynolds number the effect of the moment of inertia of the body and the motion of the freely falling wings. The result is that the non-dimensional autorotation frequency of a 15% thick elliptic cylinder about its center axis fixed perpendicularly to a uniform flow approaches asymptotically a constant value at sufficiently high Reynolds numbers, and that the flow pattern around a falling wing is similar to that around a wing of which axis is fixed. Lugt [*3*] studied the numerical solutions of the Navier-Stokes equations and described the autorotation phenomena by means of the stream lines and the equi-vorticity lines around an elliptic cylinder rotating with constant angular velocity. The Reynolds numbers of the calculated flows were limited to 200 and 400, which are far smaller than those of experimental cases. The flow around a rotating wing is characterized as an unsteady flow around a bluff body. Such phenomena have been re-

* The Institute of Space and Astronautical Science
** Department of Physics, Ochanomizu University

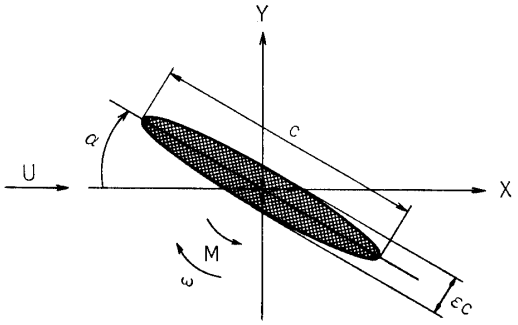

Fig. 1. Coordinate system and notation.

viewed and discussed by McCrosky [5], Barman and Graham [6], and Ericsson [7].

In this paper, the autorotation of a two-dimensional elliptic cylinder is numerically simulated by means of discrete vortex-blob method including the viscous diffusion effect. Discrete vortex method is based on the potential flow theory combined with a model of vortex generation and has been proved to be very suitable for analyzing the incompressible, high Reynolds number flow past a bluff body [8]. The autorotation frequencies and the flow patterns resulted were compared with those by the experiments using a wind tunnel and a water channel. The experiments were carried out in both of the autorotating state and the forced rotating state with the constant angular velocity driven by a stepping motor.

Figure 1 gives the coordinate system. The elliptic cylinder with the chord length of c, the thickness ratio ε and the moment of inertia I is rotating clockwise in the uniform flow with the speed of U. The rotational angle (or angle of attack) of the cylinder is measured clockwise starting from the x-axis, and ω is the angular velocity of it and M is the counter-clockwise rotational moment acting on it. Three non-dimensional parameters characterizing this phenomenon are defined as: the Reynolds number $\mathrm{Re}=Uc/\nu$, the spin parameter (or the non-dimensional frequency) $S=c\omega/2\pi U$, and the non-dimensional moment of inertia of the cylinder $I^*=32I/\pi\rho c^4$, where ν and ρ are the kinematic viscosity and the density of the fluid, respectively. That is, I^* represents the ratio of the moment of inertia of the body to that of the circular cylinder of fluid with the diameter c. The models with smaller I^* does not autorotate in water but results in rocking motion because that the model cannot store sufficient angular momentum to overcome the retarding period.

2. Numerical Study

2.1 *Model formulation*

The equation for the angular motion of a two-dimensional elliptic cylinder rotating around its spanwise axis fixed perpendicularly to a uniform flow is

$$I\frac{d\omega}{dt}=-M-K\omega, \qquad (1)$$

where t is the time and $K(\geqq 0)$ is the coefficient of the friction or the load acting to

the body rotation. After integration with respect to α, one obtains the relation between ω and the average value of the angular velocity during one cycle $\bar{\omega}$;

$$\omega^2=\bar{\omega}^2-\frac{2}{I}\int_{\bar{\alpha}}^{\alpha}Md\alpha-\frac{2}{I}\int_{\bar{\alpha}}^{\alpha}K\omega d\alpha, \tag{2}$$

where $\bar{\alpha}$ is the angle at $\omega=\bar{\omega}$. This means that the cylinder rotates with a constant angular velocity if the moment of inertia I is large enough.

Two different techniques were used in order to analyze this problem. The first one is to calculate the average value of the aerodynamic moment, of force $\bar{M}$ acting on the cylinder, which is assumed to be rotating with a given constant angular velocity. Then the critical condition (upper limit) of the autorotation is denoted by

$$\bar{M}=0, \qquad (\partial\bar{M}/\partial\omega)_{\bar{M}=0}>0. \tag{3}$$

The second method is to solve Eq. (1) by numerical integration under a given finite moment of inertia. A pursuit of motion results in either autorotating state or rocking motion while eventually stops.

2.2 *Computational scheme*

Discrete vortex-blob method using the conformal mapping was applied for the computation. The flow quantities are made dimensionless by U and c. In particular, the dimensionless time t^* is defined as tU/c. The flow field around the rotating ellipse on the z-plane is mapped outside the static unit circle on the ζ-plane by

$$z=e^{-i\alpha}(A\zeta+B/\zeta)=G(\zeta, t), \tag{4}$$

where G denotes the mapping function with

$$A=(1+\varepsilon)/4, \qquad B=(1-\varepsilon)/4. \tag{5}$$

The complex velocity potential F expressing the flow field, which is impulsively started from rest, at the time step N is given by

$$F_N=A(e^{-i\alpha}\zeta+e^{i\alpha}/\zeta)+2\pi iABS/\zeta^2+i\sum_{k=1}^{K_N}\Gamma_{Nk}[\log(\zeta-\zeta_{Nk})-\log(\zeta-1/\bar{\zeta}_{Nk})], \tag{6}$$

where the subscript N denotes the time step, K is the total number of vortices, Γ_{Nk} and ζ_{Nk} are the strength and the position of the k-th vortex, respectively, and the over-bar indicates the complex conjugate. The induced velocity of k-th vortex is given by

$$\dot{\zeta}_{Nk}=\left[\left(\frac{\partial F_{Nk}}{\partial\zeta}\frac{\partial\zeta}{\partial z}-\frac{\partial G}{\partial t}\right)\frac{\partial\zeta}{\partial z}\right]_{\zeta=\zeta_{Nk}}, \tag{7}$$

where

$$F_{Nk}=F_N-i\Gamma_{Nk}\log(\zeta-\zeta_{Nk}). \tag{8}$$

The positions of the vortices at the next time step are determined by

$$\zeta_{N+1,k}=\zeta_{Nk}+\Delta t^*\dot{\zeta}_{Nk}, \tag{9}$$

where Δt^* is the dimensionless time step. The forces acting on the cylinder can be calculated from the unsteady Blasius formulas,

$$\begin{aligned} C_D-iC_L&=i\int\left(\frac{dF}{dz}\right)^2dz-2i\frac{d}{dt}\int\bar{z}dF,\\ C_M&=-\mathrm{Re}\int\left(\frac{dF}{dz}\right)^2zdz+\mathrm{Re}\frac{d}{dt}\int z\bar{z}dF, \end{aligned} \tag{10}$$

here Re indicates real part, C_D, C_L and C_M are the drag, lift and moment coefficients, respectively.

2.3 The boundary conditions

Strength of the newly generated vortices at each time step are determined by the no-slip condition, which introduces the viscous effect in the vicinity of the body surface. When the tangential component of the velocity difference between the ellipse and the fluid is zero, the relation is represented in the ζ-plane as follows;

$$\mathrm{Im}\left(\zeta\frac{\partial F}{\partial\zeta}\right)=\mathrm{Im}\left(\zeta\frac{\partial G}{\partial\zeta}\frac{\partial\bar{G}}{\partial t}\right),\qquad |\zeta|=1, \tag{11}$$

where Im denotes the imaginary part. Integrating between two indicated target points ζ_1 to ζ_2, one has

$$\Phi_{\zeta=\zeta_2}-\Phi_{\zeta=\zeta_1}=-\int_{\mathrm{Arg}(\zeta_1)}^{\mathrm{Arg}(\zeta_2)}\mathrm{Im}\left(\zeta\frac{\partial G}{\partial\zeta}\frac{\partial\bar{G}}{\partial t}\right)d\theta, \tag{12}$$

where $\Phi=\mathrm{Re}(F)$. It means that no net slip exists on the average sense along the element. In case of a flat plate, two discrete vortices are generated near the both edges, at which the Kutta condition is applied [9]. That is, no slip condition is adopted along the infinitesimal elements. In case of a circular cyilnder, the boundary layer along the circumference is divided into two parts and no-net-slip condition is applied along each half surface [10]. Since an elliptic cylinder has the intermediate shape between a flat plate and a circular cylinder, we set the no-net-slip condition along the partial sections around the two edges, at which two discrete vortices are generated (partition A in Fig. 2). The range of each sections are determined so as to satisfy no net slip approximately along the other sections (partition B). By using the solution of the potential flow about the rotating ellipse in the steady fluid, they, that is,

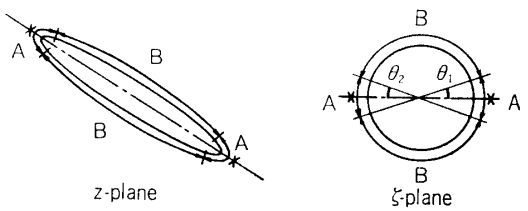

Fig. 2. Boundary conditions.

θ_1 and θ_2 on ζ-plane (in Fig. 2) are uniquely determined as the function of only the thickness ratio ε;

$$4\varepsilon(\pi/2-\theta_1)=(1-\varepsilon^2)\sin 2\theta_1, \qquad \theta_2=\theta_1 \tag{13}$$

2.4 Core of vortex-blob

The other effect of viscosity is diffusion. In order to take into account this effect, each vortex is supposed to have a viscous core, of which the radius is denoted by

$$\sigma_k=2.2418[(t_k^*+1/2St)/Re]^{1/2} \tag{14}$$

where Re is Reynolds number, t_k^* the elapsed time from the generation of the k-th vortex, and St the Strouhal number of the vortex shedding. At the generation time, each vortex is assumed to have an initial core, which touches the surface of the ellipse. When some cores are overlaped, they are supposed to be replaced by one vortex at the center of gravity. The numerical integration of Eq. (1) was done by Euler method. The computation was carried out with $\Delta t^*=0.04$. The corresponding Reynolds number is 10^5.

2.5 Results

Figure 3 shows the relation between the aerodynamic forces averaged during one cycle and the spin parameter, in which the 15% thick cylinder is rotating with constant angular velocity. The curve of C_M indicates that the 15% thick elliptic cylinder can autorotate with S=0.38 if the model has no friction or no load. When the model has finite frictional load, the zero line of C_M shifts down to the value corresponding to this load and the frequency of the autorotation is found as the intersection of the moment curve with the shifted line. If the load is so large that no intersection exists, then autorotation cannot occur. The values of C_D are almost constant against the spin parameter, whereas those of C_L increase proportionally to S except near S=0.21. We conjectured that the reason of the smaller lift at this point is due to the marging

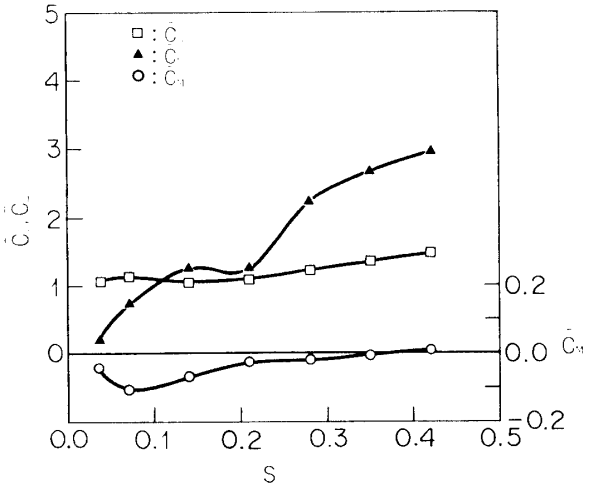

Fig. 3. Average aerodynamic forces vs. S by numerical simulation (air model).

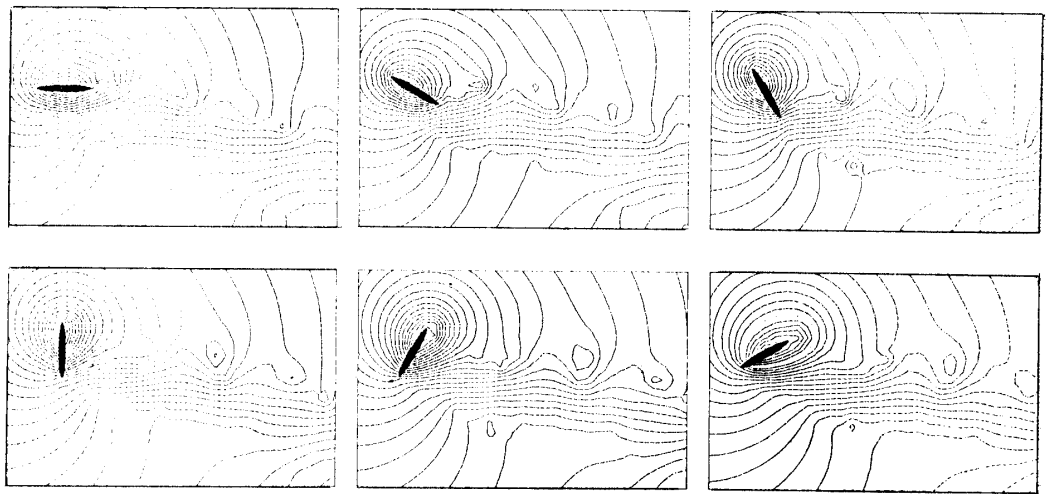

Fig. 4. Instantaneous streamlines without the uniform flow at S=0.35 at every 30° of the phase angle (air model).

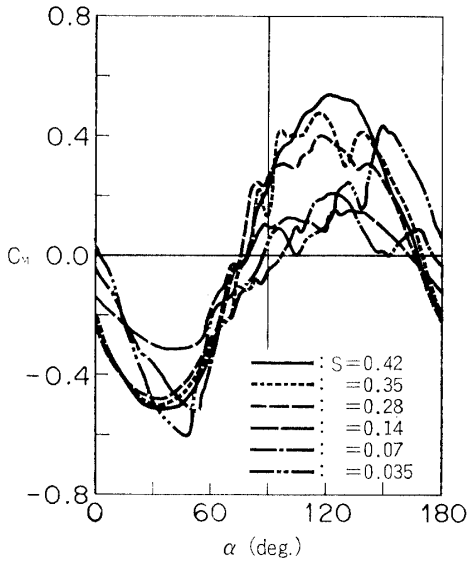

(a) moment

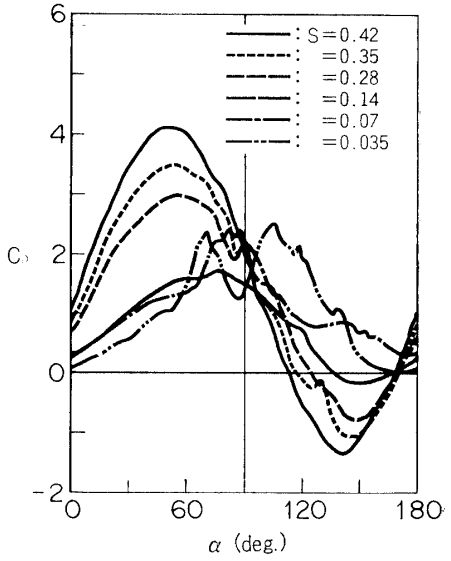

(b) drag

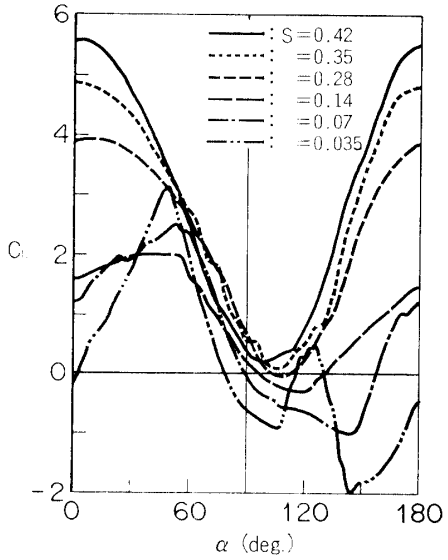

(c) lift

Fig. 5. Aerodynamic forces vs. α by numerical simulation (air model).

of the vortices behind the body. The sequence of the instantaneous streamline without uniform flow at S=0.35 is shown in Fig. 4 at every 30° of the phase angle. In Figure 5 (a), the averaged values of C_M are plotted against α. They are smaller than those predicted by the potential flow theory;

$$C_M = -\frac{\pi}{4}(1-\varepsilon^2)\sin 2\alpha \tag{15}$$

The region where C_M is positive, that is, oppose to rotation is named as the retarding period and the one where it is negative as the supporting one. As S decreases, the curve of C_M in the retarding period shifts lower and, therefore, the average value of C_M decreases. It means that the driving force is related to the vortex shedding from the retreating edge. However, when S is extremely small such as 0.035, the premature shedding introduces another growing vortex and increase C_M in the retarding period again. Figure 5 (b) shows plots of half cycle of C_D. The peak of C_D shifts down with increasing S. Figures 4 and 5 (c) denote that C_L increases as growing of the bound vortex and decreases after shedding. In case of S=0.035, the curves of C_M, C_D, and C_L has two peaks, that is, two vortices are shed during half a cycle.

Figure 6 shows the variations of the angular velocity in case with the finite moments of inertia. The amplitude of S is larger with decrease of the moment of inertia. When the angular velocity reaches zero, the cylinder begins rocking motion and eventually stops at right angle to the flow. When I^* is smaller than 0.5, the cylinder no longer autorotates. It is seen that the maximum speed point appears near 70° with decreasing I^*, and the minimum does near 160°.

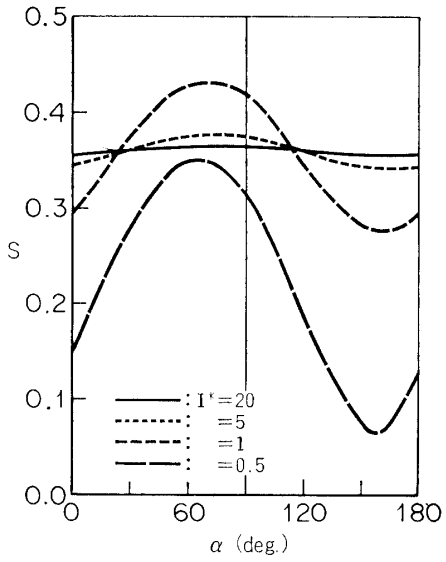

Fig. 6. Variations of ω vs. α by numerical simulation (air model).

3. Experiment

3.1 Experimental apparatus

Two kinds of the models were used. An elliptic cylinder with the chord length of 15 cm, the aspect ratio of 3, the thickness ratio of 15%, the non-dimensional moment of inertia of 20 to air flow was mounted by a ball bearing system in the wind tunnel, which has the speed range of 6 to 45 m/s. The smaller models with the chord length of 3 cm and the aspect ratio of 6 to water were mounted in the water channel, which has the speed range of 30 to 70 cm/s. Their thickness ratios and the non-dimensional moments of inertia varies from 15% to 50% and 0.7 to 2.6, respectively. The models were set either in the autorotating state or in the forced rotating state with the constant angular velocity driven by a stepping motor. In autorotating state, autorotation frequency were measured by a frequency counter triggered by a laser-photodiode system. The variation of the angular velocity of the water models was measured by using a video recording system. Flow visualization was done by smoke wire method in the air and hydrogen bubble method in the water.

3.2 Results

Figure 7 shows the relation between the Reynolds number and the autorotating frequency of air model. The values of S are kept almost constant over the high Reynolds number region. The value of $S=0.35$ corresponds that the speed of the wing edge is slightly higher than the uniform velocity ($S=1/\pi$ means that the edge speed is equal to the uniform velocity). Figure 8 shows the instantaneous streak lines around the autorotating cylinder visualized by smoke wire method at every 30° of the rotational angle. Figure 9 (a) is comparison of the flow patterns in forced rotating state with the various frequencies at $\alpha=0°$. As the frequency decreases, the vortex

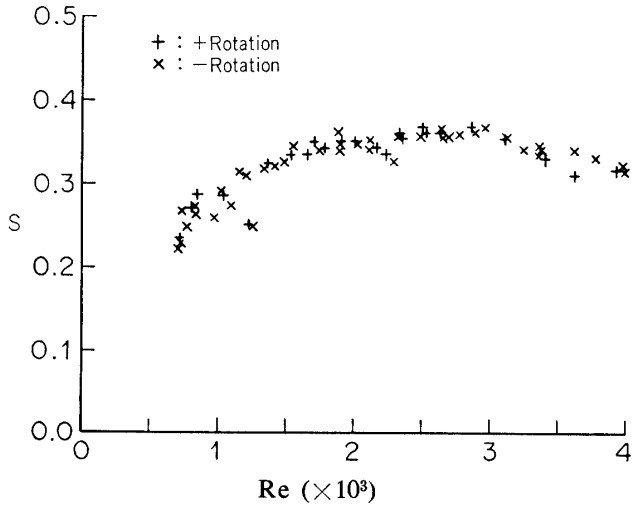

Fig. 7. Non-dimensional autorotating frequency vs. Reynolds number by experiments (air model).

shedding from the retreating edge becomes earlier. Figure 9 (b) shows the numerical results of the vortex distributions at the same condition with the experiments. The square marks denote the clockwise vortex and the × marks the counter clockwise one, representing the strength by their sizes. Figure 9 (c) shows the instantaneous streak lines originated from the same points of the smoke wires in the experiments.

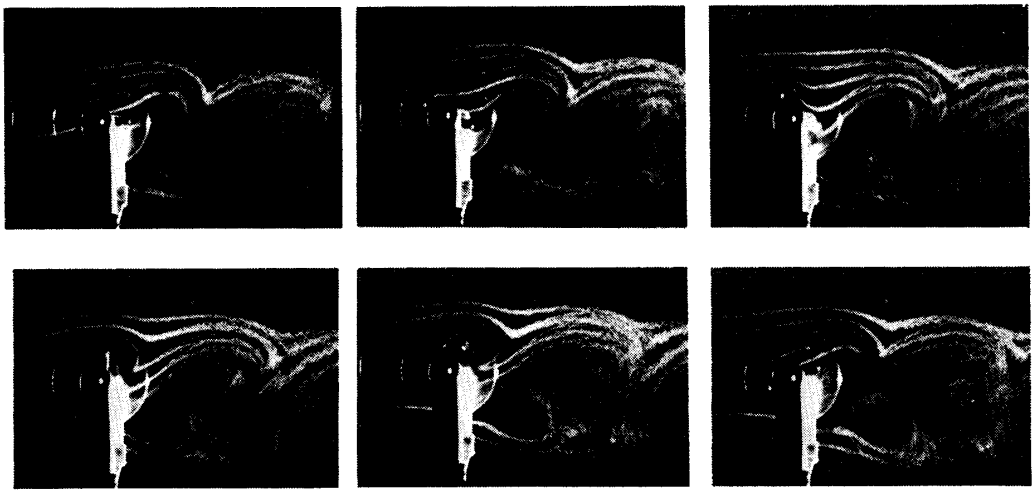

Fig. 8. Flow patterns visualized by smoke wire method in autorotating state at S=0.23 and Re=60000 at every 30° of the phase angle.

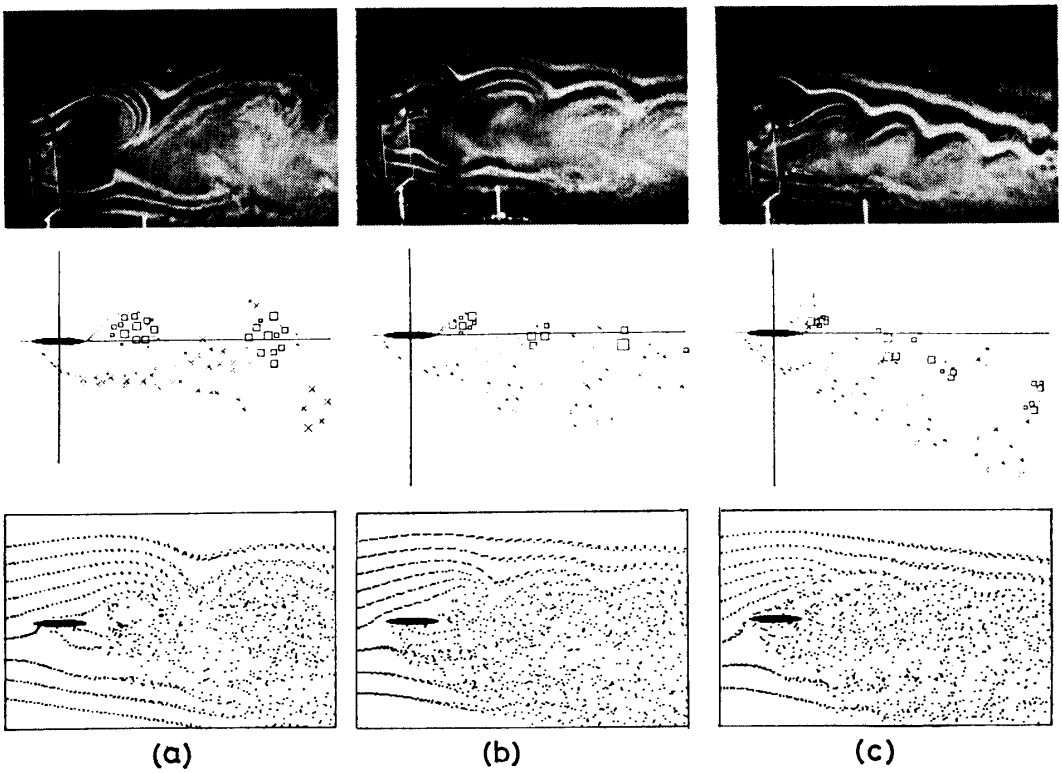

Fig. 9. Comparison of the flow patterns by the experiments, numerically simulated vortex distributions and numerically calculated streak lines, in the forced rotating state. S=0.14 (a), 0.28 (b), 0.42 (c)

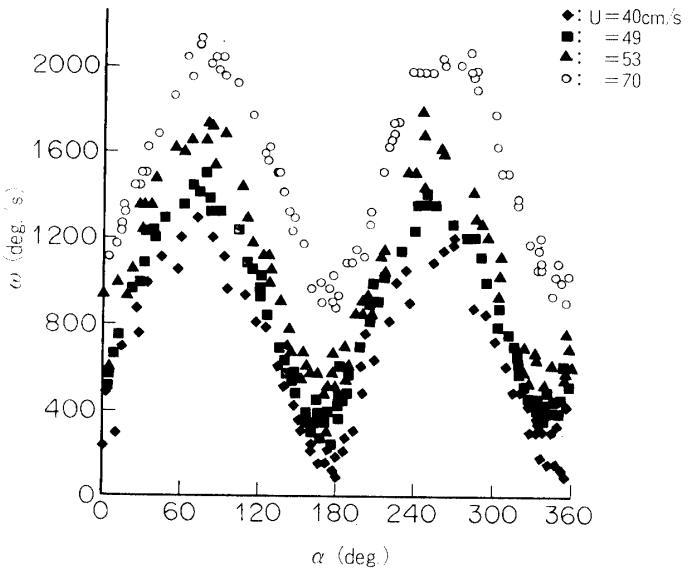

Fig. 10. Variations of ω vs. α by experiments with $\varepsilon=0.2$ and $I^*=0.89$ (water model).

The agreement between the numerical and the experimental results are good. Down wash becomes stronger as the frequency increases.

In Fig. 10, the variation of the angular velocity versus α is plotted in various flow speeds in water with the small moment of inertia ($I^*=0.89$). Figure 11 (a) is the photographs of flow visualization in water in the autorotating state and in the forced rotating state with the constant angular velocity. The numerical results corresponding to these are shown in Fig. 11 (b) with the instantaneous streamlines and the vortex distributions at $\alpha=0°$ and 90°. These figures show that the vortex shedding from the retreating edge is delayed as compared with the constant angular velocity state because of the fast rotation near the right angle of attack position in the small moment of inertia. The rotating frequency is quickly lowered as I^* decreases less than 1 in Fig. 6.

4. Discussions

4.1 Mechanism of autorotation

When the moment of inertia of the cylinder is large enough, the driving force of autorotation is explained as follows: The suction effect due to a strong bound vortex growing at the retreating edge favors rotation during the supporting period, whereas this supporting torque changes into adverse torque during the retarding period. When S is larger than the value at the critical condition of autorotation (upper limit), the vortex shedding is delayed because of fas rotation, while it produces adverse torque. Therefore the average value of torque becomes positive. On the contrary, when S is small, the premature shedding reduces the adverse torque and made the average value negative. When S is much smaller, the vortex shedding does not synchronize with rotation. Then the average torque becomes positive again. Hence, the driving torque derives from shedding of a strong vortex clinging behind the retreating edge.

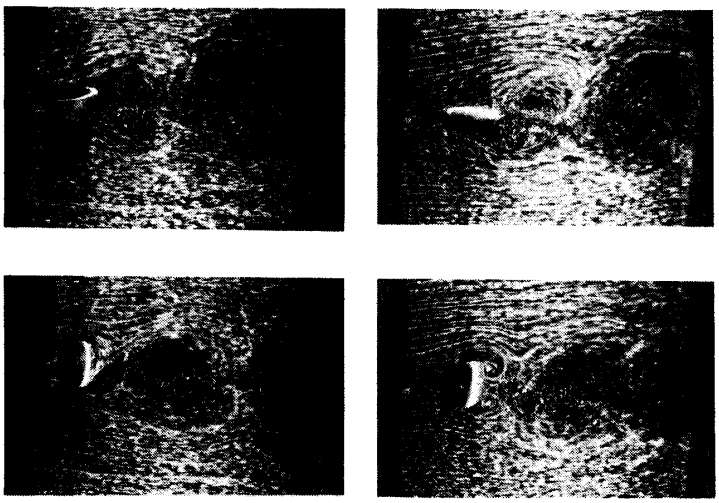

Autorotation Forced Rotation

(a) Experiments with $I^*=0.89$ (water model)

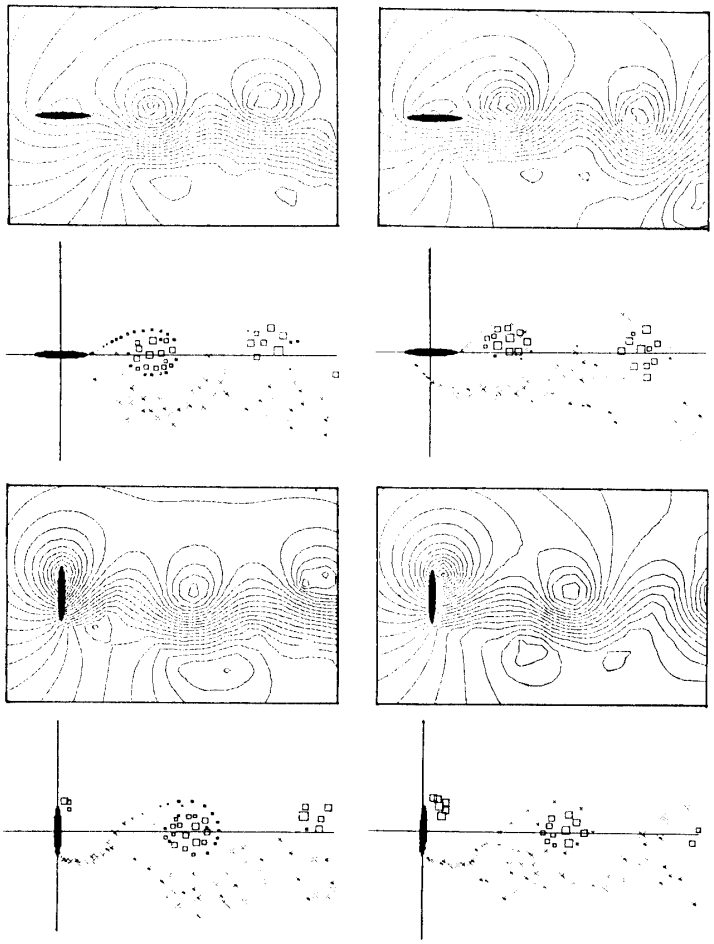

Autorotation Forced Rotation

(b) Numerically simulated streamlines and vortex distributions with $I^*=0.5$ (air model)

Fig. 11. Comparison of the flow patterns at $\bar{S}=0.14$ in the autorotating state and in the forced rotating state.

4.2 Effect of the moment of inertia

When I^* is small, the angular velocity at near the right angle to the flow becomes larger and the vortex shedding is delayed. Then the average torque increases, and the average angular velocity reduces, as shown in Fig. 6. Figure 12 shows plots of the average non-dimensional frequency $\bar{S}$ versus I^*. In case of air model ($Re=10^5$) the cylinder cannot autorotate with the value of I^* less than 0.5. The differences between the results of the computation and the experiments are supposed due to the frictional load around the axis. The 50% model indicates the higher value of the critical moment of inertia. Some computations for $Re=12000$ corresponding water model were carried out and the result indicates the qualitative difference caused by the Reynolds number difference.

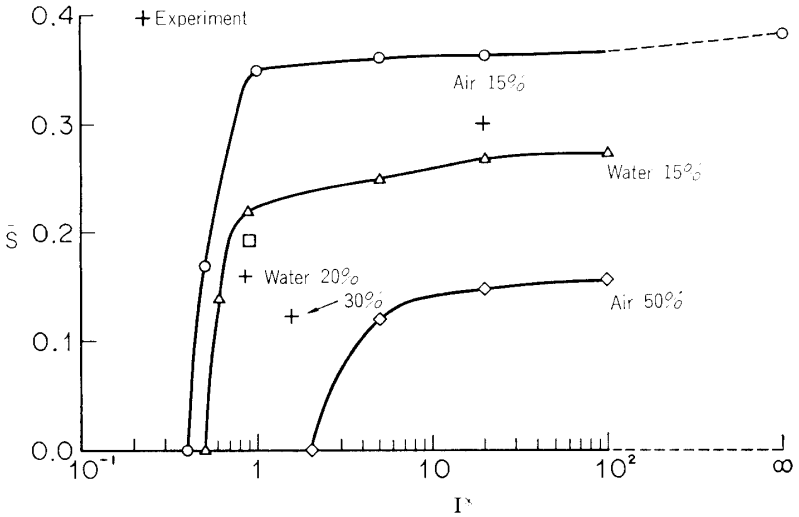

Fig. 12. Effect of I^* on $\bar{S}$; Air and Water correspond to $Re=10^5$ and $Re=12000$, respectively.

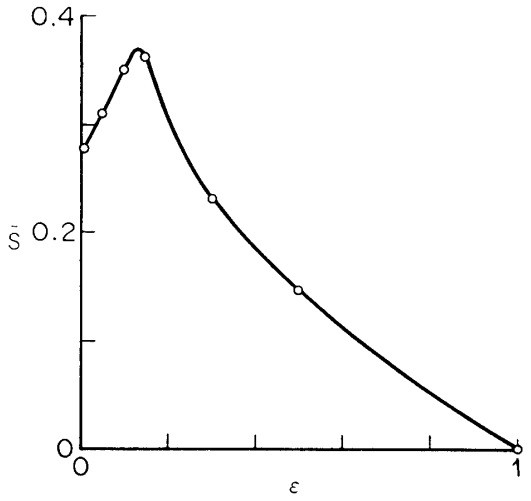

Fig. 13. Effect of ε on $\bar{S}$ predicted by numerical simulation (air model).

4.3 Effect of the thickness ratio

The effect of thickness ratio against $\bar{S}$ are seen in Fig. 13. The smaller thickness ratio results in faster rotational speed, however the 13% thick elliptic cylinder can autorotate faster than a flat plate. The reason is supposed to be the synchronization of the vortex shedding from the advancing edge.

5. Conclusion

Autorotation in high Reynolds number flows was investigated and it is concluded as follows:

(1) The critical condition of autorotation was determined by the numerical simulation as $S=0.38$ with the large moment of inertia, and gives a good argreement with the results of experiments.

(2) The driving force of autorotation comes from the synchronized shedding of a strong vortex clinging behind the retreating edge with rotation.

(3) The critical moment of inertia was determined as $I^*=0.5$ with 15% thick elliptic cylinder in the high Reynoles number flow. It increases with increasing the thickness ratio.

(4) The 13% thick elliptic cylinder can autorotate faster than a flat plate,

Acknowledgements

The authors would like to express their appreciation to Professor K. Oshima and Professor K. Kuwahara for many fruitful discussions.

References

[*1*] E. H. Smith, J. Fluid Mech. **50** (1971), 513.
[*2*] J. D. Iversen, J. Fluid Mech. **92** (1979), 327.
[*3*] H. J. Lugt, J. Fluid Mech. **99** (1980), 817.
[*4*] H. J. Lugt, Ann. Rev. Fluid Mech. **15** (1983), 123.
[*5*] W. J. McCroskey, J. Fluids Eng., Transactions of ASME **99** (1977), 8.
[*6*] P. W. Bearman and J. M. R. Graham, J. Fluid Mech. **99** (1980), 225.
[*7*] L. E. Ericsson, AIAA Journal **18** (1980), 935.
[*8*] A. Leonard, J. Comp. Phys. **37** (1980), 289.
[*9*] K. Kuwahara, J. Phys. Soc. Japan **35** (1973), 1545.
[*10*] K. Kuwahara, J. Phys. Soc. Japan **45** (1978), 292.